PAPER

Check for updates

Identifying mechanistic differences between co-fed CO_2 hydrogenation and reactive CO_2 capture using Ru and Pd dual function materials

Chae Jeong-Potter, [ID] *† Neha Mehra, [ID] Carrie A. Farberow [ID] and Daniel A. Ruddy [ID] *

Dual function materials (DFMs) enable reactive carbon capture (RCkeC), an intensified approach to carbon dioxide capture and utilization for cost and energy input reductions. Yet, there is a fundamental lack of understanding of mechanisms around CO_2 adsorption and subsequent conversion on these materials, hindering further development. Herein, we investigated several supported alkaline metal oxides for their CO_2 adsorption characteristics to find that Na/Al_2O_3 had the highest CO_2 adsorption capacity, accompanied by a variety of CO_2 adsorption geometries as identified by *in situ* DRIFTS and computational modeling. The addition of catalytic metals (Ru, Pd) increased the adsorption capacity of Na/Al_2O_3 without altering binding modes. In the subsequent reactive desorption step, acetate and formate intermediates were observed. Notably, this mechanistic investigation identified that the formation of acetate species was unique to RCC on a DFM, as these species were not observed in co-fed hydrogenation over the DFM or RCC over a Na-free catalyst.

Broader context

Reactive carbon capture (RCC) seeks to address an overarching challenge in CO_2 utilization approaches: typical carbon capture and utilization (CCU) technologies require large amounts of energy for the multiple steps of purification, compression, and transportation of CO_2 after capture for conversion at a remote facility. To reduce the energy demand and break through current limitations of CCU, the RCC process instead employs dual function materials (DFMs) to enable capture and conversion in a single reactor. While recent literature has focused on the discovery of new DFM formulations and novel RCC processes, this study seeks to provide a comprehensive understanding of the key interactions between CO_2 and DFM components, and how reactive desorption mechanisms are affected. Our findings reveal that RCC catalytic mechanisms cannot be directly extrapolated from traditional co-fed hydrogenation mechanisms, providing an important learning on how the scientific community should approach the design of next generation DFMs with improved performance.

Introduction

The use of waste CO_2 as a carbon feedstock to produce fuels and chemicals through CO_2 recycling (*i.e.* capture and utilization, CCU)[1] holds great potential as a means of chemical storage to combat intermittency of renewables, a pathway commonly dubbed "power-to-X".[2–4] However, typical CCU technologies require large amounts of energy for the multiple steps of purification, compression, and transportation of CO_2 after capture for conversion at a remote facility.[5] To reduce the energy demand and break through current limitations of CCU, multifunctional materials that allow capture and conversion to occur

in a single reactor through a process dubbed reactive carbon capture (RCC) have been the topic of recent research.

One such catalytic technology platform employs dual function materials (DFMs), which are composed of sorbents and catalysts co-dispersed on the same high surface area carrier. The sorbent enables selective capture of CO_2 from a gas stream (including dilute CO_2 concentrations) and the catalyst component subsequently converts the adsorbed CO_2 upon introduction of a reactive gas (typically H_2) *in situ*.[6–8] The product from the most established DFM, comprised of Ru and/or Ni with an alkaline sorbent, is methane *via* the CO_2 methanation reaction.[9,10] While renewable methane would be an excellent transition fuel that can leverage currently available infrastructure, it is economically noncompetitive relative to inexpensive fossil methane (averaging \$2.19 per MMBTU in 2024 in the US[11]). These challenges motivate the design and investigation of DFMs that enable CO_2 capture and conversion to more valuable and more useful C1

National Laboratory of the Rockies, Catalytic Carbon Transformation and Scale-Up Center, Golden, Colorado, 80401, USA. E-mail: dan.ruddy@nlr.gov

† Present address: Department of Biomedical and Chemical Engineering, Syracuse University, Syracuse, New York, 13244, USA. E-mail: cjeongpo@syr.edu

products, like CO or methanol (average price of methanol was $35.66 per MMBTU in 2024[12]). These products can be used in the chemical industry or upgraded to high energy density synthetic fuels for heavy duty vehicles, marine, and aviation.

A survey of DFM formulations reveals a variety of sorbent-catalyst combinations that can perform RCC to methane, CO, and/or methanol.[8,13,14] In stark contrast to fundamental catalysis science and mechanistic studies of conventional co-fed CO_2 hydrogenation reactions (which include the Sabatier reaction, $CO_2 + 4H_2 \rightarrow CH_4$; reverse water gas shift, $CO_2 + H_2 \rightarrow CO$; and methanol synthesis, $CO_2 + 3H_2 \rightarrow CH_3OH$),[15–20] there is a lack of depth in the fundamental understanding of how CO_2 binds to DFMs, and importantly, how the subsequent mechanisms during reactive desorption are affected. Furthermore, recent explorations of novel DFMs to achieve more valuable C1 products like MeOH have shown that co-fed CO_2 hydrogenation activity does not necessarily directly translate to RCC performance, suggesting that there are important mechanistic differences between the two modes of operation.[21] Such differences were also suggested by Moreno Bravo et al., when studying Ru DFMs composed of rare earth oxides.[22] While possible mechanisms over DFMs have been proposed,[23–25] a systematic study is needed to understand: (1) the role of the alkali sorbent site in CO_2 binding, (2) the subsequent effect of catalyst metal identity on the resulting transformation of the adsorbed CO_2, and (3) the differences in adsorbed intermediates between the RCC and co-fed hydrogenation mechanisms.

Herein, we first characterized several Al_2O_3-supported sorbents for their capacity and CO_2 binding geometries. We then characterized Ru and Pd DFMs with the same sorbent component (motivated by the breadth of RCC and co-fed CO_2 hydrogenation literature around these two catalytic metals) to determine the effect of the metal catalyst on CO_2 capacity and binding, followed by operando DRIFTS characterization of observable intermediates during simulated reactive desorption. Observed CO_2 binding geometries and resulting intermediates were further verified through molecular modeling. Comparisons between co-fed hydrogenation over the Ru DFM and RCC on Na-free Ru/Al_2O_3 identified that the formation of acetate surface species was unique to RCC on the DFM.

Experimental

Material synthesis

Supported sorbents were prepared by introducing alkali (Na, K) and alkaline earth (Mg, Ca) metal oxides via incipient wetness impregnation of γ-Al_2O_3 (Puralox TH100/150, Sasol). Aqueous solutions of Na_2CO_3, K_2CO_3, $Ca(NO_3)_2 \cdot 4H_2O$, and $Mg(NO_3)_2 \cdot 6H_2O$ salts (Sigma Aldrich) were used for impregnation onto γ-Al_2O_3 powder to achieve a metal:Al_2O_3 molar ratio of 0.202. These salts were chosen to be representative of synthesis routes used by many previous RCC reports.[8,21,25–27] The impregnated powders were dried at 120 °C overnight (>12 h) in static air. Decomposition of the carbonate or nitrate precursors was performed using calcination at 400 °C for 4 h before characterization.

Ru and Pd DFMs were prepared by modifying Na/Al_2O_3 (prepared as described above) through incipient wetness impregnation using aqueous solutions of $Ru(NO)(NO_3)_3$ (Thermo Scientific Chemicals) and $Pd(NO_3)_2 \cdot 2H_2O$ (Sigma Aldrich) with a catalytic metal to sorbent metal molar ratio of 0.02 (equivalent to ca. 2 wt% Ru or Pd). The resulting DFMs were then dried at 50 °C overnight in static air. The catalytic metals were activated through a pre-reduction at 300 °C for 4 h in H_2 before characterization.

A non-DFM Ru/Al_2O_3 catalyst was prepared in the same manner by utilizing an aqueous solution of $Ru(NO)(NO_3)_3$ for impregnation of γ-Al_2O_3. The sample was dried at 120 °C overnight in static air and activated through a pre-reduction at 300 °C for 4 h in H_2.

Characterization

CO_2 and CO chemisorption were measured using an Autosorb-1C gas sorption analyzer (Quantachrome Instruments). Approximately 100–150 mg of material was diluted with 1 g of quartz chips in a u-shaped analysis tube. For CO_2 chemisorption, sorbent materials were calcined at 400 °C in N_2 for 8 h, and DFMs were reduced at 300 °C in H_2 for 8 h. The sample was then evacuated for 8 h prior to analysis. CO_2 chemisorption was measured at 100, 200, and 300 °C between 80 and 760 Torr in 50 Torr increments. The site density of strong CO_2 chemisorption was determined by the difference of the total and weak isotherms, extrapolated to zero pressure. For CO chemisorption, DFMs were reduced at 300 °C in H_2 for 4 h, followed by evacuation for 8 h prior to analysis. CO adsorption isotherms were measured at 40 °C between 80 and 760 Torr in 50 Torr increments. The site density of total CO uptake from the combined isotherm, extrapolated to zero pressure, was used to determine the average particle size of Ru and Pd. A metal (M) to CO binding stoichiometry, M:CO, of 1.5 was used to represent the known distribution of atop (M–CO, 1:1) and bridged (M–CO–M, 2:1) CO binding on these metals. The chemisorption data has an estimated error of ±4.1% based on the reproducibility error of the calibration standard provided by Quantachrome.

DRIFTS analysis

In situ and operando diffuse reflectance infrared Fourier transform spectroscopy (DRIFTS) experiments were performed using a Thermo Scientific Nicolet iS50R FT-IR spectrometer equipped with a Harrick Praying Mantis high temperature reaction chamber attachment with CaF_2 windows. The DRIFTS spectra and backgrounds were collected at a resolution of 4 cm^{-1} with 128 scans. The samples were loaded into the sample holder on top of a small bed of quartz chips and pre-treated in situ prior to analysis. Al_2O_3-supported sorbents were calcined under flowing He for 4 h at 400 °C. DFMs and Al_2O_3-supported catalysts were reduced under flowing 50% H_2/He for 4 h at 300 °C. Backgrounds were taken at 300 °C in He and 50% H_2/He to be subtracted from the adsorption and reactive desorption steps, respectively. Flowrates were kept at 40 sccm and ramp rates at 5 °C min^{-1}, unless otherwise specified.

CO_2 adsorption was conducted at 300 °C with 5% CO_2/He for 30 min, with spectra collected in 5 min intervals. Spectra were also collected in 5 min intervals during a 1 h purge step under flowing He following the adsorption step. For *operando* analysis, reactive desorption was performed on DFMs and Al_2O_3 by switching to 50% H_2/He for 1 h, with spectra again being collected in 5 min intervals. Effluent gas of the DRIFTS cell was analyzed using a downstream on-line FT-IR (600 HSC from California Analytical Instruments) to monitor product formation.

Operando co-fed hydrogenation was conducted in the DRIFTS cell at 300 °C with a gas mixture of 10% CO_2, 40% H_2, balance He, with a background spectrum collected in 40% H_2/He. Spectra were collected after a 2-h hold at reaction conditions, after which CO_2 flow was stopped. Spectra were then collected at 5 min intervals to monitor the evolution of surface species over 1 h. Effluent gas of the DRIFTS cell was again analyzed using a downstream on-line FT-IR to monitor product formation.

Computational methods

Density functional theory (DFT) calculations were implemented using the vienna *ab initio* simulation package (VASP).[28–30] The generalized gradient approximation (GGA) through the Perdew–Burke–Ernzerhof (PBE) functional was used to approximate the exchange–correlation energy.[31,32] Electron–ion interactions were captured by projector augmented-wave (PAW) potentials, with valence wavefunctions expanded in a plane-wave basis set with an energy cutoff of 500 eV.[33] Gaussian smearing with a smearing width of 0.01 eV was employed. Spin-polarized calculations were carried out for systems involving radical adsorbates. Electronic relaxation was converged to a tolerance of 1×10^{-6} eV and the norm of force convergence was set to 0.03 eV Å^{-1}. Atomistic construction of hydrated γ-Al_2O_3 surfaces denoted as Al_2O_3-$(110)_{2H_2O}$ and $Al_2O_3(100)_{2H_2O}$ and Na-modified alumina are described in the SI.

The adsorption energy $(\Delta E_{\text{ads},i})$ for adsorbate (i) is defined as

$$\Delta E_{\text{ads},i} = E_{i/\text{slab}} - E_{\text{slab,r}} - E_{i(g)} \tag{1}$$

where $E_{i/\text{slab}}$ is the total energy of the slab with adsorbate, $E_{\text{slab,r}}$ is the energy of the relaxed slab without adsorbate, and $E_{i(g)}$ is the energy of the free, gas-phase molecule. $E_{i(g)}$ was computed by placing one "i" molecule in a $16 \times 17 \times 18$ Å^3 box. Gas-phase molecules used as reference states in this work include neutral species (CO_2, H_2O) and radical species (HCOO, CH_3COO). The corresponding optimized structures and energies are reported in Table S7 and were created using VESTA.[34]

Vibrational modes and harmonic frequencies of adsorbed species were obtained using perturbation theory without symmetry.[35] Scaling factors were not applied because the calculated scaling value for CO_2 was near unity (Table S8). Atomic simulations environment (ASE) was used to visualize and confirm the vibrational modes.[36] Frequencies for carbonate (CO_3^*) and bicarbonate (HCO_3^*) species were computed by relaxing CO_2O_s and $CO_2O_sH_s$ atoms, where 's' denotes surface atoms. Only adsorbate atoms were relaxed in vibrational calculations of CH_3COO and HCOO; all substrate atoms were fixed. Dispersion corrections to energies were not applied as this analysis focuses on

strongly chemisorbed species likely to persist at 300 °C for which binding is dictated by electrostatic interactions with the surface.

Born effective charges and the displacement vectors are used to determine the intensities (I) of infrared active vibrational modes. Intensities are calculated as

$$I(\omega) = \sum_{\alpha=1}^{3} \left| \sum_{l=1}^{M} \sum_{\beta=1}^{3} Z_{\alpha\beta}^*(l) e_\beta(l) \right|^2 \tag{2}$$

where $e_\beta(l)$ is the normalized vibrational eigenvector of the ω-th mode calculated for different atoms (l) of the system, α and β indicate the Cartesian polarizations, and $Z_{\alpha\beta}^*(l)$ is the Born effective charge tensor of the l-th atom.[37]

Results and discussion

Adsorption characteristics of Ru and Pd-based DFMs

Most DFMs employ group 1 alkali (G1-Alk) or group 2 alkaline earth (G2-Alk) metal oxides as their main sorbent component, which when dispersed on a high surface area oxide support (like Al_2O_3)[38,39] offers an intermediate CO_2 binding strength that retains CO_2 on the surface during purge and heating steps of RCC processes (*e.g.*, 200–400 °C) and is also reactive upon the introduction of H_2. Prior literature teaches that adsorption capacity, strength, and the subsequent product, can vary dramatically depending on the identity of the sorbent metal.[21,40] We began our investigation by comparing the adsorption characteristics of Al_2O_3-supported G1-Alk and G2-Alk metals, standardized by a Alk : Al_2O_3 molar ratio of 0.202, equivalent to *ca.* 10% CaO/Al_2O_3, a standard weight loading used in recent DFM reports (elemental analysis reported in Table S1). Chemisorption analysis with the *in situ* DRIFTS spectra for this series of sorbents (Fig. S1) revealed Na/Al_2O_3 has the highest gravimetric adsorption capacity, the greatest efficiency in terms of molar adsorption capacity, and a diversity of CO_2 binding modes (Fig. S2). As previous RCC reports also commonly chose Na as the sorbent material,[27,41–44] Na/Al_2O_3 was selected in this work as the most interesting candidate for a deeper spectroscopic study.

It is noted that there is currently no clear agreement in DFM literature on the exact structure and phase of alumina-supported Na species; however, we are able to speculate that the majority of Na sites are well dispersed based on our chemisorption and DRIFTS data. First, following analysis by Keturakis *et al.*, we believe to be at just below a monolayer of Na. Keturakis *et al.* ascribed 5% "Na_2O" as the weight loading for monolayer formation on 200 m^2 g^{-1} γ-Al_2O_3, resulting in a Na density of 5.11 Na atoms per nm^2.[39] Our DFMs contain 2.7 wt% Na (3.6% "Na_2O") on 142 m^2 g^{-1} γ-Al_2O_3, resulting in 4.8 Na atoms per nm^2. These materials are below the expected monolayer coverage, which would favor high dispersion of Na species after activation. We consider that Na is likely to exist in a combination of oxide or hydroxide forms (NaO_x, $NaAlO_x$, NaOH) and form surface carbonates and/or bicarbonates upon CO_2 adsorption. Stoichiometrically, this would result in molar capacities (mol$_{CO_2}$ mol$_{Na}^{-1}$) ranging from 1 (1 : 1 Na : CO_2 binding, as in $NaHCO_3$ or $NaAlCO_3(OH)_2$ formation) to 0.5 (2 : 1 Na : CO_2, as in

Na_2CO_3 formation) in a perfectly dispersed material. Comparatively, Na/Al_2O_3 exhibited a strong chemisorption capacity of 0.22 mol_{CO_2} mol_{Na}^{-1} at 100 °C which we equate to between 22 and 44% dispersion, indicating that there may a portion of clustered, inaccessible Na sites or the existence of lower binding strength sites that do not strongly bind CO_2 at 100 °C. Realistically, our DRIFTS data (Fig. S2c) at 300 °C showed a mixture of polydentate ($Na:CO_2 > 2$) carbonates, conceptually favored by larger Na (or Na-O-Al) clusters, as well as bridged bidentate ($Na:CO_2 = 2$) and chelating bidentate ($Na:CO_2 = 1$) carbonates, favored by smaller particles. Thus, Na speciation is likely a mixture of well-dispersed oxides and hydroxides with some portion that is either inaccessible in clusters or binds CO_2 too weakly.

Na/Al_2O_3 was modified with two representative CO_2 hydrogenation catalysts, Ru and Pd. Ru is commonly used in DFM formulations to achieve methanation, showing excellent redox behavior (*i.e.*, rapid reduction following oxidation) and long-term stability.[26,27] Pd is a versatile metal that catalyzes reverse water gas shift (RWGS) and methanol formation from CO_2, and we employ it here to study CO formation over a DFM.[45–47] The catalysts were introduced *via* serial incipient wetness impregnation, targeting a molar ratio of catalyst : sorbent metal of 0.1, resulting in *ca.* 2 wt% target loading (analyzed to be 2.3% Ru and 2.5% Pd). After reduction at 300 °C, CO chemisorption at 40 °C was employed to determine the average particle sizes. As expected, the low wt loadings resulted in small average particle sizes of 0.70 and 1.1 nm for $Ru+Na/Al_2O_3$ and $Pd+Na/Al_2O_3$, respectively. We note that DFMs for CO and MeOH synthesis based on Cu are exciting new additions to the RCC field,[21] but these are less well understood compared to Ru- and Pd-based DFMs, and thus, are not the most suitable catalysts for the goals of this study.

The strongly chemisorbed CO_2 on the resulting DFMs (termed, $Ru+Na/Al_2O_3$ and $Pd+Na/Al_2O_3$) were quantified over a range of temperatures (Fig. 1A). At all adsorption temperatures, the DFMs displayed enhanced adsorption capacity relative to the metal-free Na/Al_2O_3 (Fig. 1B). The Ru-DFM exhibited a greater increase in strong CO_2 chemisorption which was

attributed to two factors: (i) the reported behavior of Ru to promote the decomposition of Na_2CO_3 precursor salts during DFM pretreatment, activating more Na adsorption sites,[25,48] and (ii) additional CO_2 adsorption on Ru/RuO_x during the capture step. Considering these two factors for the Pd-DFM, the more modest increase in CO_2 adsorption capacity *versus* Na/Al_2O_3 may be caused by a combination of less effective participation of Pd to activate Na sites during pretreatmentrelative to Ru and a limited CO_2 adsorption on Pd/PdO_x surface species, which has been described to be nondissociative and weak.[49,50]

Characterization of CO_2 binding geometries on Ru- and Pd-DFMs was performed through *in situ* DRIFTS. The resulting spectra after pre-treatment, CO_2 exposure, and He purge are displayed in Fig. 2 with the spectrum after CO_2 adsorption on Na/Al_2O_3 included for comparison. The broad absorbances observed were deconvoluted to make precise peak assignments, associate them to adsorption geometries (Table 1), and detect any perturbations resulting from the presence of a catalytic metal. We note that exact assignment between chelating and bridged bidentate carbonate geometries to the peaks fit at 1618/1311 cm^{-1} and 1669/1378 cm^{-1} on the Na/Al_2O_3 – which we will refer to as CO_3^*(B-I) and CO_3^*(B-II), respectively – is difficult as metrics for determining the strength of binding were found to be contradictory. For instance, CO_3^*(B-II), located at higher wavenumbers and showing the greatest decrease in intensity after an inert purge (Fig. S2), would be expected to correspond to a weaker bound bidentate geometry. Yet, the $\Delta\nu_3$ splitting of the CO_3^* (B-II) species – a heuristic that can be used to determine the strength of surface carbonate binding – is lower at 291 cm^{-1} compared to 307 cm^{-1} of the CO_3^*(B-I) species, indicating a marginally stronger bound species. It is more conservative to conclude that these bidentate geometries are quite similar in binding strength and refrain from making exact assignments based on this dataset. Peaks at 1554 and 1340 cm^{-1} correlated to a polydentate geometry (CO_3^*(P)), and a small shoulder at 1755 cm^{-1} corresponded to Na_2CO_3 nanoparticles.[39]

Further understanding of potential CO_2 binding geometries on Na/Al_2O_3 was obtained through DFT calculations. Na/Al_2O_3
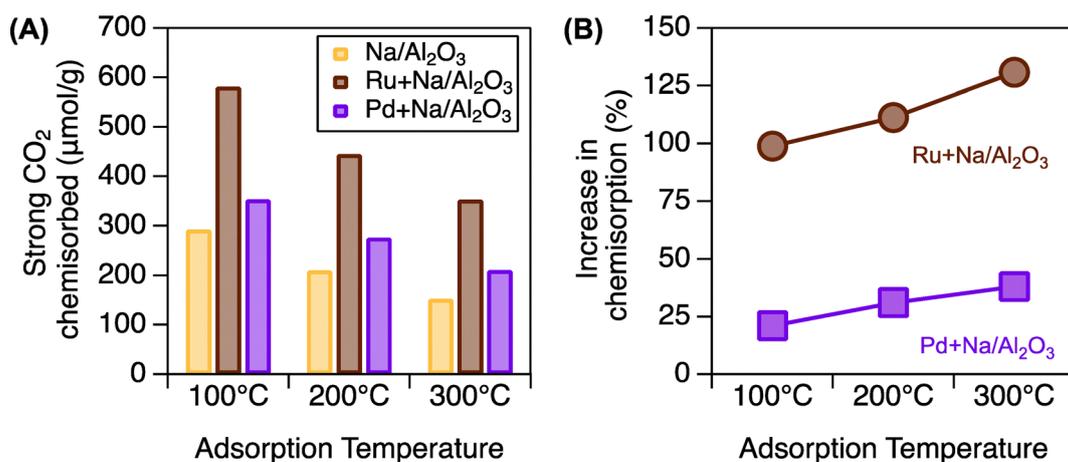
Fig. 1 (A) Strong CO_2 chemisorption for Na/Al_2O_3 (yellow), $Ru+Na/Al_2O_3$ (brown), and $Pd+Na/Al_2O_3$ (purple) over a range of adsorption temperatures (100–300 °C). (B) Percent increase in strong CO_2 chemisorption compared to Na/Al_2O_3.

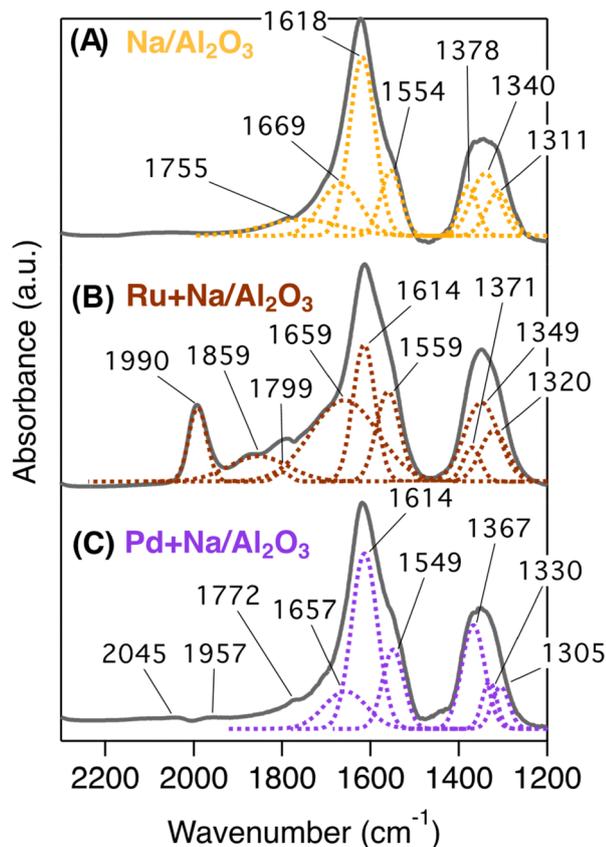**Fig. 2** *In situ* DRIFTS spectra of (A) Na/Al$_2$O$_3$, (B) Ru+Na/Al$_2$O$_3$, and (C) Pd+Na/Al$_2$O$_3$ after 30 min adsorption with 5% CO$_2$/He and 30 min purge with He at 300 °C. Catalyst-containing samples were reduced for 4 h in 50% H$_2$/He at 300 °C before analysis; Na/Al$_2$O$_3$ was pre-treated for 4 h in He at 400 °C. Larger formatting is provided in SI (Fig. S3).

Table 1 Assignments of observed peaks in DRIFTS spectra of Na/Al$_2$O$_3$, Ru+Na/Al$_2$O$_3$, and Pd+Na/Al$_2$O$_3$ after 30 min of adsorption (5% CO$_2$/He at 300 °C), followed by an inert purge in He (displayed in Fig. 2). Asymmetric and symmetric vibrational splitting is also reported ($\Delta\nu_3$)

Surface species	Na/Al$_2$O$_3$	Ru+Na/Al$_2$O$_3$	Pd+Na/Al$_2$O$_3$
CO$_3$* (B-I)	1618 cm^{-1}	1614 cm^{-1}	1614 cm^{-1}
	1311 cm^{-1}	1320 cm^{-1}	1305 cm^{-1}
	($\Delta\nu_3$ = 307 cm^{-1})	($\Delta\nu_3$ = 294 cm^{-1})	($\Delta\nu_3$ = 309 cm^{-1})
CO$_3$* (B-II)	1669 cm^{-1}	1659 cm^{-1}	1657 cm^{-1}
	1378 cm^{-1}	1371 cm^{-1}	1367 cm^{-1}
	($\Delta\nu_3$ = 291 cm^{-1})	($\Delta\nu_3$ = 288 cm^{-1})	($\Delta\nu_3$ = 290 cm^{-1})
CO$_3$* (P)	1554 cm^{-1}	1559 cm^{-1}	1549 cm^{-1}
	1340 cm^{-1}	1349 cm^{-1}	1330 cm^{-1}
	($\Delta\nu_3$ = 214 cm^{-1})	($\Delta\nu_3$ = 211 cm^{-1})	($\Delta\nu_3$ = 219 cm^{-1})
Carbonyls	—	1990 cm^{-1}	2045 cm^{-1}
		1859 cm^{-1}	1957 cm^{-1}
		1799 cm^{-1}	

models were constructed by adding a Na$_2$O molecule to γ-Al$_2$O$_3$ surfaces (Al$_2$O$_3$(110)$_{2H_2O}$ and Al$_2$O$_3$(100)$_{2H_2O}$, Fig. S4–S6, Table S2). We note that simulations of CO$_2$ bound to Al$_2$O$_3$(110)$_{2H_2O}$ and Al$_2$O$_3$(100)$_{2H_2O}$ showed reasonable agreement between the computed IR spectra of various CO$_2$ binding geometries and the observed spectra on γ-Al$_2$O$_3$ (Fig. S7 and Table S3). In the most stable configurations, Na$_2$O on Al$_2$O$_3$(110)$_{2H_2O}$ and Al$_2$O$_3$(100)$_{2H_2O}$

transformed to Na$_2$O(H) through migration of a H* from a surface Al-hydroxyl group (Fig. S8). Simulated IR spectra of unique CO$_2$ adsorption geometries, varying in CO$_2$ coordination to surface Na, Al, or to both Na and Al surface atoms on Na/Al$_2$O$_3$ models (Table S4), showed that various bicarbonate, bidentate, and polydentate species were well-aligned with the experimental spectrum (Fig. S9).

The spectra of both DFMs show broad absorbances at 1700–1500 cm^{-1} and 1400–1300 cm^{-1}, similar to Na/Al$_2$O$_3$, with minor perturbations to the exact peak locations. On Ru+Na/Al$_2$O$_3$, the symmetric vibration of the CO$_3$*(B-I) species (lower wavenumber peak) shifted, resulting in a $\Delta\nu_3$ splitting value of 294 cm^{-1}, compared to 307 cm^{-1} on the Na/Al$_2$O$_3$, indicating a marginally stronger carbonate-surface binding strength. CO$_3$*(B-II) peaks both shifted to lower wavenumbers, with a $\Delta\nu_3$ value of 288 cm^{-1} (291 cm^{-1} on Na/Al$_2$O$_3$). The CO$_3$*(P) shifted to higher wavenumbers, yielding a similar $\Delta\nu_3$ value of 211 cm^{-1} for Ru-DFM compared to 214 cm^{-1} for Na/Al$_2$O$_3$. The Ru-DFM also displayed strong interactions between Ru and carbonyl species, presumably formed from CO$_2$ dissociation during the adsorption step, as evidenced by the complex feature between 2000 and 1750 cm^{-1}. We attributed peaks observed at 1990 and 1799 cm^{-1} to a mixture of linear, di-, and bridged carbonyls on Ru.[51] The additional peak at 1859 cm^{-1} could be attributed to a Ru carbonyl that is further stabilized by the presence of Na species. Such phenomenon has been reported with other noble metals (*e.g.*, Au, Pd), where the presence of Na$^+$ (and other alkali metal cations) induced red-shifted IR peaks of carbonyls associated with the noble metal site.[52] We further confirmed this assignment using CO DRIFTS at 300 °C on Ru+Na/Al$_2$O$_3$ and Na-free Ru/Al$_2$O$_3$ (Fig. S10), which revealed a peak near 1850 cm^{-1} only on the Ru+Na/Al$_2$O$_3$ material.

For Pd+Na/Al$_2$O$_3$, no major perturbations were detected for the CO$_3$*(B-I) peak locations (1614/1305 cm^{-1} *versus* 1618/1311 cm^{-1} on Na/Al$_2$O$_3$), preserving a $\Delta\nu_3$ value of 309 cm^{-1}. A greater shift was observed on the CO$_3$*(B-II) species to lower wavenumbers as also observed on the Ru-DFM. The CO$_3$*(P) peaks shifted to lower wavenumbers as well; however, neither shifts associated with the two geometries resulted in significant differences to the splitting values. The Pd component of the DFM also exhibited interactions with *in situ* generated CO, as detected by peaks at 2045 and 1957 cm^{-1}.[53] Based on the low peak intensities, however, these Pd-(CO)$_x$ species are much less abundant than for Ru+Na/Al$_2$O$_3$, consistent with prior reports of low CO$_2$ and CO binding energy on Pd.[49,50]

Reactive desorption over DFMs and sorbent-free catalysts

The subsequent transformation or decomposition of the surface carbonates during a simulated reactive desorption step (*i.e.*, hydrogenation) of an RCC cycle were monitored using *operando* DRIFTS. Following the adsorption and purge steps as outlined in the previous section, 50% H$_2$/He was introduced to the DRIFTS reactor at ambient pressure. Upon the introduction of H$_2$ to the CO$_2$-laden Ru+Na DFM (Fig. 3A), there was rapid consumption of the Ru-carbonyls, CO$_3$*(B-II), and CO$_3$*(B-I) species, correlated with a sharp rise in the signal for gas-phase CH$_4$ in the reactor effluent (Fig. 3B). The carbonyl and
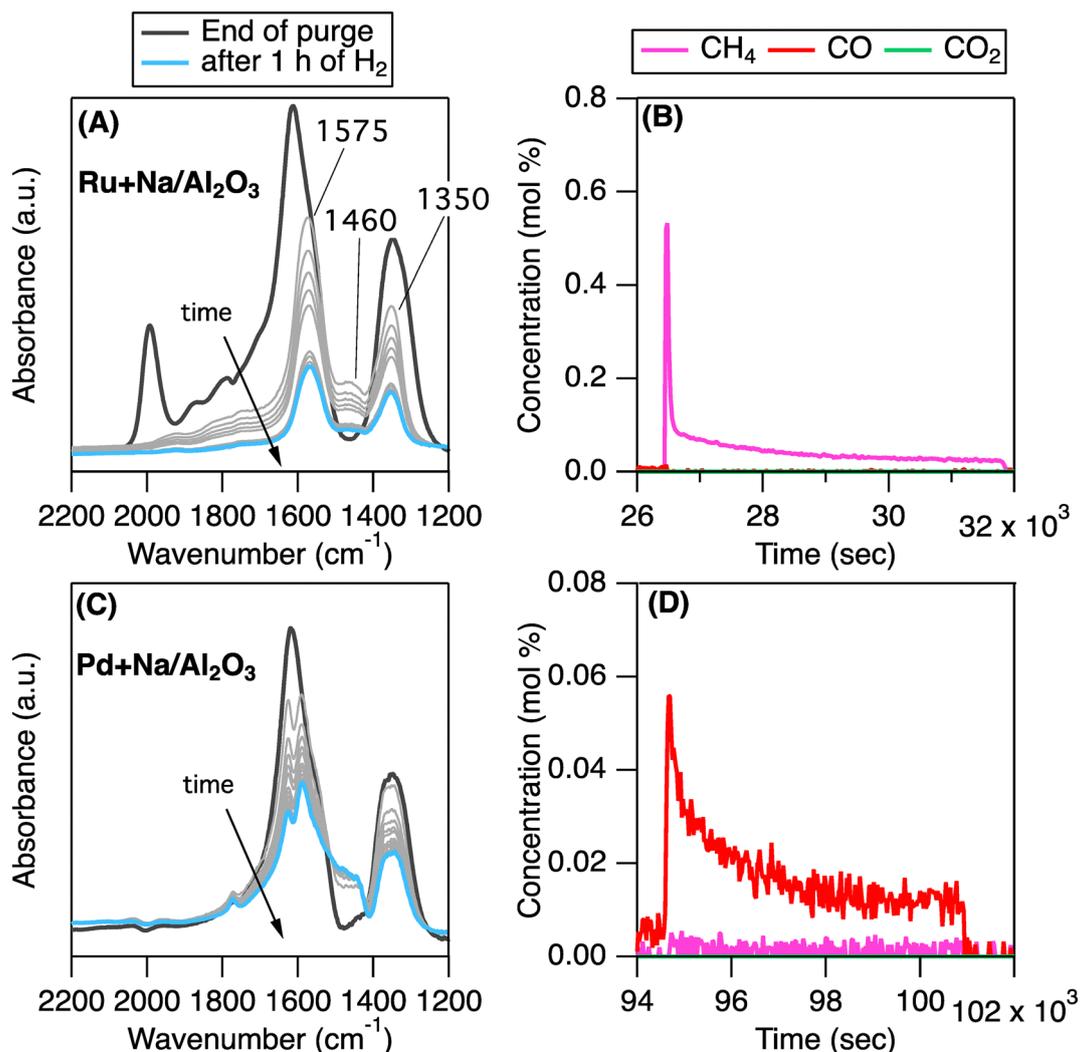
Fig. 3 DRIFTS spectra of reactive desorption following CO_2 adsorption and inert purge (as seen in Fig. 2) on (A) Ru+Na/Al_2O_3 and (C) Pd+Na/Al_2O_3 with accompanying downstream product analysis, (B) and (D), respectively. Dark gray spectra were taken at the end of a 30 min He purge following the CO_2 adsorption step; light gray spectra were taken following exposure to H_2 in 5 min intervals; and blue spectra were taken after 1 h of continuous H_2 exposure. All steps were carried out at 300 °C.

carbonate species were almost fully consumed by the end of H_2 exposure (1 h), and the Ru+Na DFM maintained selective production of CH_4 without any CO observed. A peak at 1460 cm^{-1} also rapidly formed upon the introduction of H_2, presumably associated with an intermediate species. While this species was largely consumed, some small fraction persisted at the end of H_2 exposure, along with peaks at $\sim$1575 and $\sim$1350 cm^{-1}. Based on literature reports for traditional CO_2 methanation over a Ru/Al_2O_3 catalyst (i.e., not a DFM and not operated with a cyclic CO_2–H_2 feed), an Al_2O_3-associated formate (HCOO*) intermediate would be expected, exhibiting peaks at 1593, 1392, and 1375 cm^{-1}.[15] The observed peaks here do not align with these expected wavenumber positions, and with CO_2 binding dominated at Na sites as indicated by the data in Fig. S2, we do not expect an HCOO*-Al intermediate to form under these reaction conditions. Instead, it may be possible that a formate is associated with the Na sites. Previous reports assign Na-formate with peaks at 1620–1567 and

1366–1377 cm^{-1}, which would lie under the large peaks observed in our spectra, and are also in the range for polydentate surface carbonates noted above.[54] Thus, an exact assignment for a Na-formate species is difficult. Further identification of the observed intermediate(s), including those associated with 1460 cm^{-1}, was explored with computational modeling (vide infra). As mentioned, the peaks at 1575, 1350, and 1460 cm^{-1} persist at low intensities even after 1 h of reactive desorption, indicating that the Na sites that are occupied by the associated intermediates are not available for CO_2 adsorption in subsequent cycles. This is in line with the larger DFM literature, which often show a decrease in CO_2 adsorption capacity in the first few cycles. It is worth noting, however, that extended aging studies of Ru+Na DFMs have been well reported, showing no decrease in methanation activity over 50+ cycles under "clean CO_2" adsorption conditions (i.e., no contaminants such as H_2O and O_2 present).[27] We thus believe that the residual build up of intermediates observed here would

neither cause cycle-to-cycle deactivation in the studied conditions nor hinder the mechanistic characterization presented in this work.

The simulated reactive desorption step progressed similarly on Pd+Na/Al$_2$O$_3$, with the introduction of H$_2$, there was a sharp and selective release of CO (Fig. 3C and D), correlated with the initial rapid consumption of each surface carbonate species. However, even after 1 h of H$_2$ exposure, a large portion of the observed peak intensity for surface carbonates remained. It is expected that the kinetics for CO production are slow at this low temperature of 300 °C, since thermodynamics dictate that the RWGS reaction is generally operated above 400 °C. With the persistence of the carbonate species, it is difficult to clearly identify specific intermediate structures that may lie under those peaks. However, a broad peak around 1460 cm^{-1} appeared rapidly with the introduction of H$_2$, indicative of a surface intermediate similar to that formed on the Ru+Na DFM. It has been proposed that the mechanism of CO$_2$ hydrogenation on Pd/Al$_2$O$_3$ progresses through a CO* intermediate (derived from other intermediates such as formate[47,53] or carboxyl[45]). Here, we observed that adsorption of CO on Pd is not favored (as evidenced by the low intensity of peaks between 2100 and 1900 cm^{-1}), likely resulting in desorption of gaseous CO (the major product) rather than further hydrogenation of CO* to CH$_3$OH or CH$_4$.

On both DFMs, the peak at 1460 cm^{-1} may correlate best with a surface acetate intermediate (CH$_3$COO*), reported to form by reaction between hydroxyl groups (OH*) and carbonyls (CO*), hydrogenation of CO* (to form H–C–O* intermediates), or between CO* and methyl groups (CH$_3$*).[55–57] Interestingly, acetate intermediates are more often associated with CO methanation or Fischer–Tropsch rather than CO$_2$ methanation, which we also confirmed by comparing DRIFTS spectra during co-fed CO$_2$ hydrogenation and CO hydrogenation over non-DFM Ru/Al$_2$O$_3$ (Fig. S11); importantly, a 1460 cm^{-1} peak was only observed during CO hydrogenation. To further confirm the assignment of an acetate species, DFT calculations were performed to compute infrared active bands of acetate and formate adsorbed on Na-free (Fig. S12, Table S5) and Na-modified hydrated alumina surfaces (Fig. S13, Table S6). Stable adsorbed acetate and formate species on Na/Al$_2$O$_3$(110)$_{2H_2O}$ are shown in Fig. 4A–F. Acetates coordinated at Na, both Na and Al, and Al (Fig. 4A–C, respectively), all displayed vibrational signatures between 1400 and 1500 cm^{-1}, corresponding well to the observed 1460 cm^{-1} peak. Among the computed species, Al-coordinated CH$_3$COO* was the most stable (−1.99 eV, Table S6) and formed chelating bidentate motifs, exhibiting major peaks at 1530 and 1462 cm^{-1} associated with v_{as}(OCO) vibration and v_s(OCO) stretch mixed with CH$_3$ bending, respectively. The bridged acetates coordinated to two surface Na sites and that coordinated to a Na and Al site exhibited peaks at 1448 and 1430 cm^{-1}, respectively, indicating that there is likely a mixture of CH$_3$COO* geometries and site coordination. In contrast, HCOO*—regardless of coordination and geometry—did not display bands in the 1400–1500 cm^{-1} range (Fig. 4D–F), further corroborating that the observed 1460 cm^{-1} peak in the DRIFTS spectrum can be assigned to a surface acetate. Formates did, however, exhibit peaks at ca. 1600 and ca. 1350 cm^{-1}, corresponding well to the 1575 cm^{-1} and 1350 cm^{-1} envelopes observed in DRIFTS. HCOO* geometries also had adsorption
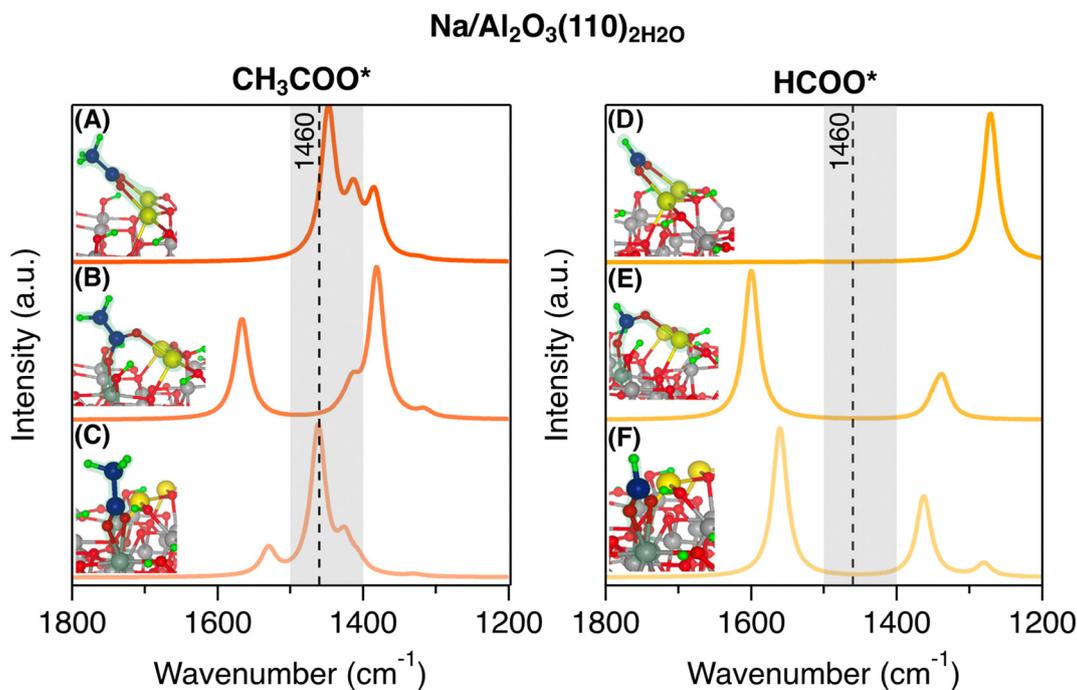

Fig. 4 Computed vibrational spectra and images of the corresponding structures for Na-coordinated, Na, Al-coordinated, and Al-coordinated acetate (CH$_3$COO*) (A–C, respectively) and formate (HCOO*) (D–F, respectively) on Na/Al$_2$O$_3$(110)$_{2H_2O}$. A black dashed line indicates the 1460 cm^{-1} wavenumber observed in the simulated RCC experiment. Atom colors: O-red, Al-grey, H-green, C-dark blue, Na-yellow.

energies similar to CH_3COO* (Table S6), indicating that they would be stable on the DFM surface and suggesting that they are likely present in the observed DRIFTS spectra. It is worth mentioning that $CO_3*(P)$ species were also assigned to similar wavenumbers (1559/1349 cm^{-1}); however, we conclude that their contributions are likely minor compared to that of the hydrogenated intermediates, given that their calculated adsorption energies are notably higher (−0.99 eV *versus* −1.99 eV, Table S4). In summary, experimentally observed envelopes at 1575, 1460, and 1350 cm^{-1} during reactive desorption correlated well with predicted IR active modes of adsorbed CH_3COO* and $HCOO*$, verifying the formation and presence of these key intermediates during RCC.

As evidenced in the DRIFTS spectra, the Na sorbent sites in these DFMs dominate the interactions with CO_2. To understand differences between surface species and reactive intermediates with and without Na sorbent sites, RCC on a Na-free Ru/Al_2O_3 catalyst was probed with DRIFTS (Fig. 5). After CO_2 exposure (green spectrum, Fig. 5A), the DRIFTS spectrum exhibited a sharp peak at 2042 cm^{-1}, which is assigned to linear atop $CO*$ species on Ru.[58] Notably, the peak associated with Na-stabilized Ru carbonyl species (1859 cm^{-1}, Fig. 2B) was not observed, further supporting our initial assignment of this peak to the presence of Na species. Further, the complex envelope between 1650 and 1200 cm^{-1} was distinct in shape compared to that on the Ru+Na DFM, and indicated various Al_2O_3-carbonate structures: (i) a bicarbonate species (HCO_3*) designated by peaks at 1648, 1439, and 1228 cm^{-1}, (ii) a monodentate species indicated by a peak at 1520 cm^{-1}, and (iii) a formate species, likely formed by interaction between bicarbonate species and residual $H*$ on the catalyst surface persisting after pre-reduction, designated by peaks at 1590, 1392, and 1375 cm^{-1}, all in accordance with reported peak positions for these surface species. After a He

purge (dark gray spectrum, Fig. 5A), the intensity of all peaks decreased; in particular, the peaks associated with the bicarbonate species were no longer detectable, indicating complete desorption of this surface species that is critical to RCC performance. The remaining peaks correspond to formate and monodentate species.

Upon exposure to H_2 (Fig. 5B), the carbonyl 2042 cm^{-1} peak rapidly decreased, and in its place, peaks at 2040, 2006, and 1970 cm^{-1} appeared. While there was a significant decrease in the intensities of these new peaks, 2040 and 1970 cm^{-1} features persisted even after 1 h of H_2 exposure. According to a previous report by Wang *et al.*, these peaks can be associated with geminal di-carbonyl species on low coordination Ru sites and are designated as a spectator species during CO_2 methanation.[15,59] Thus, the decrease in the peak intensities detected here can be described as a simple desorption of the carbonyl species, rather than consumption for conversion to CH_4. The remaining features, associated with formate and monodentate carbonate species, were consumed almost to completion during the H_2 exposure.

The geometries and activity of adsorbed CO_x species are considerably altered by the presence of Na sites. On the Ru+Na DFM, Na dominates as the primary adsorption site, offering strongly bound (but chemically reactive) bidentate and polydentate carbonate structures, compared to weakly bound bicarbonate and monodentate geometries on Al_2O_3 that desorb before reactive desorption begins. The presence of Na also impacts the distribution of carbonyl species, largely evidenced by a peak at *ca.* 1850 cm^{-1} that only appears on the Ru+Na DFM; notably, all carbonyls on the Ru+Na DFM are reactive and produce CH_4, compared to the persistence of an unreactive geminal di-carbonyl on the Na-free Ru/Al_2O_3. Lastly, acetate emerges as a key intermediate in the presence of Na, compared to formates on a Na-free Ru/Al_2O_3, likely as a result of the
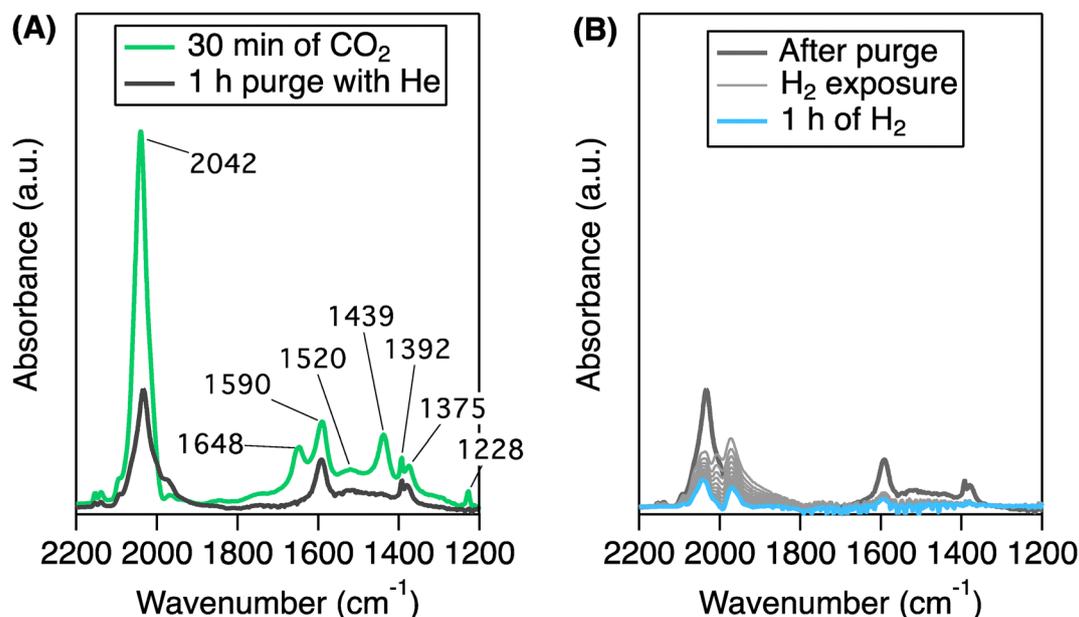
Fig. 5 DRIFTS spectra of Ru/Al_2O_3 (A) after 30 min of CO_2 exposure followed by a 1 h purge with He and (B) reactive desorption in H_2 at 300 °C.

different coverage and distribution of carbonyls on the two surfaces.

Ultimately, we are able to provide insight on the mobility of surface species in RCC. It is debated whether RCC mechanisms are driven by CO_2 desorption/re-adsorption, CO_3^* migration, or H^* migration. We hypothesize that migration of a variety of surface species may occur under these conditions. We observed that the formation of reactive hydrogenated intermediates (*e.g.*, acetate, formate) is rapid and associated with the Na sorption site, likely driven by the migration of H^* from Ru active sites to surface carbonates on the Na site. As proposed in co-fed CO_2 hydrogenation, formates likely undergo hydrogenation to CO^*, which migrate to Ru sites for further hydrogenation to CH_4. Additionally, CO^* and CH_x^* form acetates that can occupy diverse Na and Al site types and form a relatively more stable intermediate. These reported surface phenomena are coupled with no CO_2 slip (*i.e.*, no detection of gas phase CO_2), further reducing the probability that CO_2 is desorbed into the gas phase to be readsorbed to the surface for reaction (*i.e.*, CO_2 desorption/re-adsorption mechanism).

The migration of intermediates could also conceptually coincide with the migration of active phases (*i.e.*, Ru and Na species). Based on the fact that water is formed during the CO_2 hydrogenation reaction (co-fed or RCC), one would presume that Na species hydrate and dehydrate through the course of the reaction. The Na–O–Na dimer (as depicted in Fig. S8) may disperse to two adjacent NaOH species when hydrated and migrate to similar alumina surface sites. This migration would theoretically depend on the binding energy of NaOH to alumina and proximity of other alumina sites and may be aided by surface hydration, where Na^+ moves from one bound water site to another with protons moving in the other direction. As this concept pertains to acetate/formate surface migration, similarly,

one must consider binding energy, proximity of Na binding sites for migration, and species moving in the opposite direction for charge balance. Mechanistically, Na migration and acetate/formate migration are completely independent of each other. Na sites may be strongly bound to the alumina surface or may move with acetate/formate, and one would presume that protons are the charge compensating species moving in the other direction. Yet, regardless of whether the intermediates traverse in the bound state or in the ionic state, the ultimate result is that they must traverse close to a Ru site to be further reacted.

Proposed mechanistic differences between reactive desorption and co-fed hydrogenation over Ru+Na/Al$_2$O$_3$

To investigate potential differences in the reaction mechanisms of CO_2 methanation during RCC cycles compared to co-fed hydrogenation, a mixed stream of CO_2 and H_2 was fed over Ru+Na/Al$_2$O$_3$ in the DRIFTS reactor cell. The DRIFTS spectra after 2 h of reaction at 300 °C and a CO_2:H_2 ratio of 1:4 are displayed with the black solid line in Fig. 6A, and the corresponding effluent gas analysis is presented in the blue region of Fig. 6B. Several differences in surface species populations were notable in the spectrum after 2 h of co-fed reaction compared to RCC reactive desorption. In the co-fed condition, the carbonate envelopes were centered at 1604 and 1340 cm^{-1} (compared to 1650 and 1350 cm^{-1}), indicating a different distribution of carbonate species during co-fed hydrogenation. Also, a set of triplet peaks between 3000 and 2600 cm^{-1} corresponded well with the C–H bond of a Na-formate species (NaOOCH).[54] These triplet peaks were not observed in the previous reactive desorption experiment (comparison in Fig. S14), and coupled with the shift in the carbonate envelopes, formates appear to be abundant. The carbonyl region was also distinct with higher
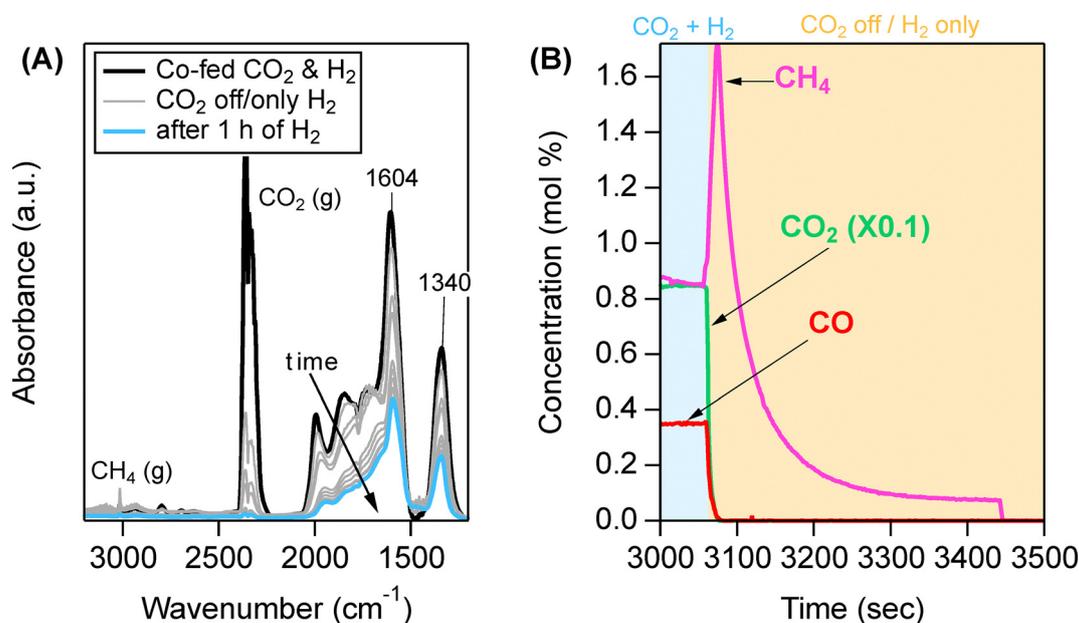

Fig. 6   (A) *In situ* DRIFTS spectra on Ru+Na/Al$_2$O$_3$ during co-fed hydrogenation (CO_2:H_2 = 1:4, 10% CO_2, 40% H_2, balance He) at 300 °C and subsequent hold in H_2 without CO_2. (B) Gas-phase product detection during experiment.

intensity peaks in the lower wavenumber region (1850–1750 cm^{-1}), indicating a higher surface population of bridged carbonyls on Ru.

A particularly clear difference was the absence of a peak at 1460 cm^{-1}, indicating that the corresponding acetate intermediate observed during reactive desorption was not formed/stabilized during co-fed hydrogenation. Importantly, the different surface speciation led to a different product distribution (Fig. 6B). During co-fed hydrogenation (blue region), a mix of CO and CH$_4$ was detected, in stark contrast to the high selectivity to CH$_4$ observed during RCC reactive desorption. After 2 h of co-fed CO$_2$ and H$_2$, the flow of CO$_2$ was stopped, and the DRIFTS spectra and product evolution were continuously monitored under flowing H$_2$ (Fig. 6A, gray spectra, Fig. 6B, yellow region). Upon the change in reactant gas flow, there was significant consumption of the surface species and a slight increase in intensity at 1460 cm^{-1} (zoom on region in Fig. S15), accompanied by a rapid decrease in the signals for CO$_2$ and CO, and rapid, selective formation of CH$_4$, mirroring the evolution of products during RCC reactive desorption.

The evolution of surface species during co-fed hydrogenation and reactive desorption over a Ru+Na/Al$_2$O$_3$ is summarized in Fig. 7. In co-fed CO$_2$ methanation over Ru+Na/Al$_2$O$_3$, the Na component dominates interactions with CO$_2$ (i.e., not Al$_2$O$_3$ as observed on Na-free Ru/Al$_2$O$_3$), wherein the CO$_2$ was found to adsorb as surface carbonates (CO$_3$*). The formation of HCOO* was also observed during the co-fed reaction, presumably as CO$_3$* are hydrogenated by Ru-activated H*, following hypotheses that Al–HCO$_3$* species are hydrogenated to HCOO*.[15] A high surface coverage of Ru–CO* groups was observed, mostly in the linear and bridged configurations, and there was a notable absence of unreactive gem-dicarbonyls over this DFM.

Under RCC conditions, CO$_2$ also preferentially adsorbed onto Na sites as CO$_3$* species. Additionally, it adsorbed as CO* on Ru sites, though in lower abundance compared to co-fed hydrogenation. Once H$_2$ was introduced, CO* and some CO$_3$* species were rapidly consumed. It is likely that the CO$_3$* species were hydrogenated via H* from Ru, much like in co-fed hydrogenation, to form a formate intermediate. However, a distinct peak at 1460 cm^{-1} indicates the formation of an acetate intermediate, assigned through computational modeling and CO methanation experiments. This is likely formed between CH$_x$* and CO* species as reported for CO methanation and based on our reaction conditions.[55] The acetate species is consumed, albeit slowly, and forms methane with high selectivity. Falbo et al. reported that acetates on Ru/Al$_2$O$_3$ started decomposing at 250 °C, supplying CO* to the surface.[55] Furthermore, Na-acetate has been reported to decompose to form methane in biomass hydrotreating applications.[60] Thus, it is likely that the surface Na-acetate formed under RCC conditions also decomposes to form methane, given that the reactive desorption step is carried out at 300 °C. We propose that the formation of this acetate species contributes to the high methane selectivity in reactive desorption: in the co-fed environment, there is a constant population of CO* occupying the Ru sites which must also activate H$_2$. To activate H$_2$, some CO must desorb, resulting in the observed CO in the product stream, and thus, a lower CH$_4$ selectivity. However, in RCC reactive desorption, the CO* on Ru is quickly reacted or drawn away to form acetate species, liberating Ru sites for H$_2$ activation. The acetate species then serve as a temporary reservoir of CO* species for hydrogenation when more hydrogenating sites are available, accompanied by liberating an equivalent of CH$_4$
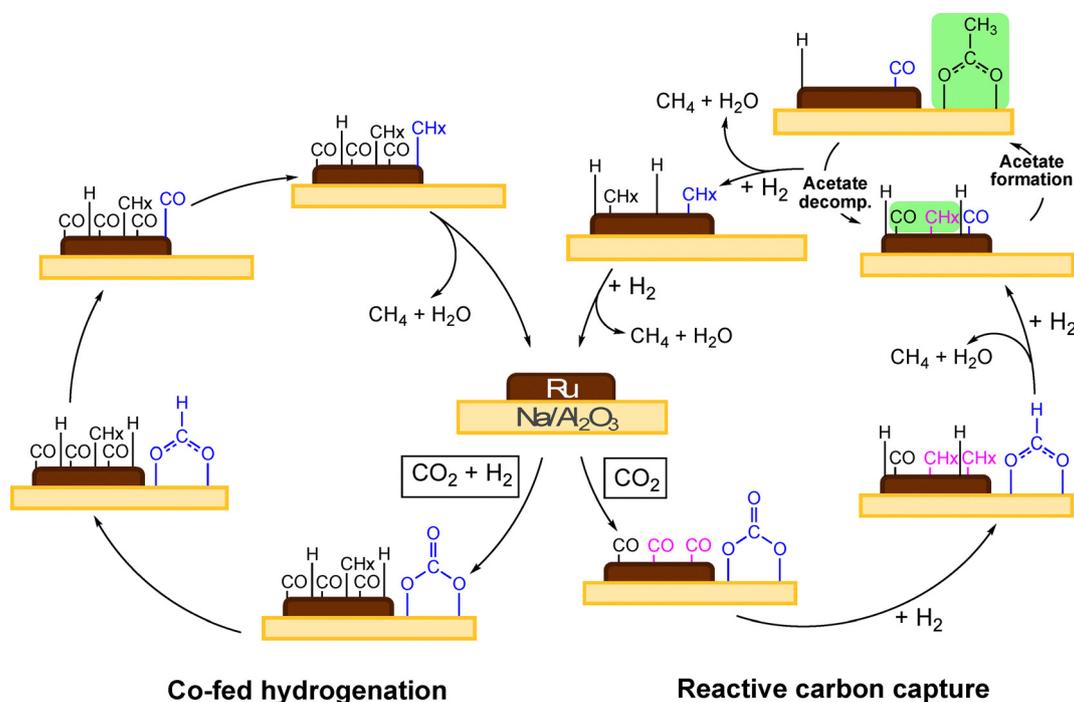

Fig. 7 Schematic of surface species evolution in co-fed hydrogenation and reactive carbon capture over a Ru+Na/Al$_2$O$_3$ DFM.

when they decompose. The net result is no desorption of CO and high methane selectivity.

Conclusions

This work provides a comprehensive understanding of the key interactions between CO_2 and DFM components – sorbent and catalytic metal – and how reactive desorption mechanisms proceed over a Ru+Na DFM. We first investigated the CO_2 adsorption characteristics on several Al_2O_3-supported group 1 and group 2 metal oxides, which showed that Na/Al_2O_3 maintains the highest gravimetric and molar adsorption capacity over a range of flue gas temperatures and adsorbed CO_2 in diverse geometries (bidentate, polydentate, bicarbonate). Catalytic metals (Ru, Pd) introduced to Na/Al_2O_3 generally increased adsorption capacity, with the greatest increase on Ru, and without major perturbation of adsorbed CO_2 binding geometries on Na sites. In subsequent reactive desorption on the DFMs, $Ru+Na/Al_2O_3$ selectively produced CH_4 while $Pd+Na/Al_2O_3$ selectivity produced CO, indicating tunability of product selectivity subject to catalytic metal. Through *operando* DRIFTS and computational modeling, formate and acetate species were identified as likely intermediates on both DFMs. Comparison of RCC over a Na-free Ru/Al_2O_3 showed that Na plays a key role in stabilizing carbonates and altering the distribution of carbonyls. Notably, (i) carbonates species bind stronger on $Ru+Na/Al_2O_3$, (ii) the acetate intermediate was only detected on $Ru+Na/Al_2O_3$, and (iii) unreactive geminal di-carbonyls were only formed on Ru/Al_2O_3. Finally, a bound acetate intermediate does not persist under co-fed conditions over $Ru+Na/Al_2O_3$, accompanied by lower selectivity to CH_4 when compared to RCC. We posit that the acetate species during RCC draw CO* species away from Ru sites during RCC, which are required for hydrogen activation, leading to selective CH_4 formation. In summary, we propose that the characteristics and relative populations of adsorbed CO_x species are affected by (1) the presence of strongly basic sites in DFMs when compared to sorbent-free catalysts, and (2) the step-wise introduction of CO_2 and H_2 compared to co-fed CO_2 and H_2. The unique synergy between the DFM materials properties and RCC process operation thus results in a reaction mechanism and catalytic performance that cannot be directly extrapolated from traditional co-fed hydrogenation literature.

Conflicts of interest

There are no conflicts to declare.

Data availability

The following data are included in the supplementary information (SI): metal content, CO_2 chemisorption data, and DRIFTS analysis of adsorbed CO_2 for sorbents; structural models of slabs and adsorbed CO_2 used in computational analyses; computed vibrational spectra for adsorbed CO_2 and related species; additional *in situ* DRIFTS data on DFMs with relevant

time-dependent spectra; surface energies of various slab terminations. See DOI: https://doi.org/10.1039/d5ey00320b. All computational files have been made freely available at: C. Jeong-Potter, N. Mehra, C. A. Farberow and D. A. Ruddy, Identifying mechanistic differences between co-fed CO_2 hydrogenation and reactive CO_2 capture using Ru and Pd dual function materials, *Materials Cloud Archive*, 2026, **32**, https://doi.org/10.24435/materialscloud:nr-g4.

References

1 IPCC, in *Special Report: Global Warming of 1.5 °C*, 2018.

2 S. Stucki, A. Schuler and M. Constantinescu, *Int. J. Hydrogen Energy*, 1995, **20**, 653–663.

3 C. Graves, S. D. Ebbesen, M. Mogensen and K. S. Lackner, *Renewable Sustainable Energy Rev.*, 2011, **15**, 1–23.

4 F. V. Vázquez, J. Koponen, V. Ruuskanen, C. Bajamundi, A. Kosonen, P. Simell, J. Ahola, C. Frilund, J. Elfving, M. Reinikainen, N. Heikkinen, J. Kauppinen and P. Piermartini, *J. CO$_2$ Util.*, 2018, **28**, 235–246.

5 M. Fasihi, O. Efimova and C. Breyer, *J. Cleaner Prod.*, 2019, **224**, 957–980.

6 M. S. Duyar, M. A. Arellano and R. J. Farrauto, *Appl. Catal., B*, 2015, **168**, 370–376.

7 M. S. Duyar, S. Wang, M. A. Arellano-treviño and R. J. Farrauto, *J. CO$_2$ Util.*, 2016, **15**, 65–71.

8 I. S. Omodolor, H. O. Otor, J. A. Andonegui, B. J. Allen and A. C. Alba-Rubio, *Ind. Eng. Chem. Res.*, 2020, **59**, 17612–17631.

9 S. Wang, R. J. Farrauto, S. Karp, J. H. Jeon and E. T. Schrunk, *J. CO$_2$ Util.*, 2018, **27**, 390–397.

10 M. A. Arellano-treviño, N. Kanani, C. W. Jeong-potter and R. J. Farrauto, *Chem. Eng. J.*, 2019, **375**, 121953.

11 U.S. Energy Information Administration, Henry Hub Natural Gas Spot Price, https://www.eia.gov/dnav/ng/hist/rngwhhdm.htm, (accessed 16 July 2025).

12 Methanex, Historical Methanol Posted Price, https://www.methanex.com/our-products/about-methanol/pricing/, (accessed 16 July 2025).

13 P. Melo Bravo and D. P. Debecker, *Waste Disposal Sustainable Energy*, 2019, **1**, 53–65.

14 S. B. Gharamaleki, T. R. Reina and M. S. Duyar, *Prog. Energy*, 2025, **7**, 012001.

15 X. Wang, Y. Hong, H. Shi and J. Szanyi, *J. Catal.*, 2016, **343**, 185–195.

16 M. A. Nolen, S. A. Tacey, S. Kwon and C. A. Farberow, *Appl. Surf. Sci.*, 2023, **637**, 157873.

17 M. A. Abir, R. E. Phillips, J. Z. M. Harrah and M. R. Ball, *Catal. Sci. Technol.*, 2024, **14**, 4506–4521.

18 C. Zhang, Z. Xiao, X. Guo, X. Tan, J. Gu, J. Li, G. Li, J.-J. Zou and D. Wang, *Chem. Eng. J.*, 2025, **519**, 165414.

19 R. Ye, J. Ding, T. R. Reina, M. S. Duyar, H. Li, W. Luo, R. Zhang, M. Fan, G. Feng, J. Sun and J. Liu, *Nat. Synth*, 2025, **4**, 288–302.

20 A. J. Al Abdulghani, S. Ganguly, R. H. Hagmann, Z. Sun, M. Alvear, L. O. Mark, E. Nikolla, Y. J. Pagán-Torres and I. Hermans, *J. Am. Chem. Soc.*, 2025, **147**, 27438–27448.

21 C. Jeong-Potter, M. A. Arellano-Treviño, W. W. McNeary, A. J. Hill, D. A. Ruddy and A. T. To, *EES. Catal.*, 2024, **2**, 253–261.

22 L. Moreno Bravo, F. C. Meunier and J. Kopyscinski, *Appl. Catal., B*, 2025, **361**, 124591.

23 L. Proaño, E. Tello, M. A. Arellano-Trevino, S. Wang, R. J. Farrauto and M. Cobo, *Appl. Surf. Sci.*, 2019, **479**, 25–30.

24 L. Proaño, M. A. Arellano-Treviño, R. J. Farrauto, M. Figueredo, C. Jeong-Potter and M. Cobo, *Appl. Surf. Sci.*, 2020, **533**, 147469.

25 S. Sapru, K. D. Hart, C. Zhou, G. Liccardo, J. Oh, M. J. Hollobaugh, J. Osio-Norgaard, A. Majumdar, B. D. Chandler and M. Cargnello, *ACS Nano*, 2025, **19**, 2484–2496.

26 M. A. Arellano-Treviño, Z. He, M. C. Libby and R. J. Farrauto, *J. CO₂ Util.*, 2019, **31**, 143–151.

27 C. Jeong-Potter, A. Porta, R. Matarrese, C. G. Visconti, L. Lietti and R. Farrauto, *Appl. Catal., B*, 2022, **310**, 121294.

28 G. Kresse and J. Hafner, *Phys. Rev. B: Condens. Matter Mater. Phys.*, 1994, **49**, 14251–14269.

29 G. Kresse and J. Furthmüller, *Phys. Rev. B: Condens. Matter Mater. Phys.*, 1996, **54**, 11169–11186.

30 G. Kresse and J. Furthmüller, *Comput. Mater. Sci.*, 1996, **6**, 15–50.

31 J. P. Perdew, K. Burke and M. Ernzerhof, *Phys. Rev. Lett.*, 1996, **77**, 3865–3868.

32 J. P. Perdew, K. Burke and M. Ernzerhof, *Phys. Rev. Lett.*, 1997, **78**, 1396.

33 P. E. Blöchl, *Phys. Rev. B: Condens. Matter Mater. Phys.*, 1994, **50**, 17953–17979.

34 K. Momma and F. Izumi, *J. Appl. Crystallogr.*, 2008, **41**, 653–658.

35 M. Gajdoš, K. Hummer, G. Kresse, J. Furthmüller and F. Bechstedt, *Phys. Rev. B: Condens. Matter Mater. Phys.*, 2006, **73**, 045112.

36 A. Hjorth Larsen, J. Jørgen Mortensen, J. Blomqvist, I. E. Castelli, R. Christensen, M. Dułak, J. Friis, M. N. Groves, B. Hammer, C. Hargus, E. D. Hermes, P. C. Jennings, P. Bjerre Jensen, J. Kermode, J. R. Kitchin, E. Leonhard Kolsbjerg, J. Kubal, K. Kaasbjerg, S. Lysgaard, J. Bergmann Maronsson, T. Maxson, T. Olsen, L. Pastewka, A. Peterson, C. Rostgaard, J. Schiøtz, O. Schütt, M. Strange, K. S. Thygesen, T. Vegge, L. Vilhelmsen, M. Walter, Z. Zeng and K. W. Jacobsen, *J. Phys.: Condens. Matter*, 2017, **29**, 273002.

37 D. Karhánek, *Self-Assembled Monolayers Studied by Density-Functional Theory*, University of Vienna, 2010.

38 P. Gruene, A. G. Belova, T. M. Yegulalp, R. J. Farrauto and M. J. Castaldi, *Ind. Eng. Chem. Res.*, 2011, **50**, 4042–4049.

39 C. J. Keturakis, F. Ni, M. Spicer, M. G. Beaver, H. S. Caram and I. E. Wachs, *ChemSusChem*, 2014, **7**, 3459–3466.

40 A. Porta, R. Matarrese, C. G. Visconti, L. Castoldi and L. Lietti, *Ind. Eng. Chem. Res.*, 2021, **60**, 6706–6718.

41 A. Bermejo-López, B. Pereda-Ayo, J. A. González-Marcos and J. R. González-Velasco, *J. CO₂ Util.*, 2019, **34**, 576–587.

42 L. Li, S. Miyazaki, S. Yasumura, K. W. Ting, T. Toyao, Z. Maeno and K. Shimizu, *ACS Catal.*, 2022, **12**, 2639–2650.

43 T. Sasayama, F. Kosaka, Y. Liu, T. Yamaguchi, S.-Y. Chen, T. Mochizuki, A. Urakawa and K. Kuramoto, *J. CO₂ Util.*, 2022, **60**, 102049.

44 L. C. Wirner, F. Kosaka, T. Sasayama, Y. Liu, A. Urakawa and K. Kuramoto, *Chem. Eng. J.*, 2023, **470**, 144227.

45 N. C. Nelson, M.-T. Nguyen, V.-A. Glezakou, R. Rousseau and J. Szanyi, *Nat. Catal.*, 2019, **2**, 916–924.

46 X. Jiang, X. Nie, X. Guo, C. Song and J. G. Chen, *Chem. Rev.*, 2020, **120**, 7984–8034.

47 X.-G. Wang, L.-Y. Qiao, L.-Y. Xu, Y.-Y. Zeng, Z.-S. Huang, S.-S. Zong, J.-X. Wang, Z.-F. Zhou and Y.-G. Yao, *Chem. Eng. J.*, 2024, **500**, 156937.

48 C. Jeong-Potter, M. Abdallah, S. Kota and R. Farrauto, *Ind. Eng. Chem. Res.*, 2022, **61**, 10474–10482.

49 F. Solymosi and A. Barko, *J. Catal.*, 1986, **101**, 458–472.

50 M. Bowker, P. Stone, R. Bennett and N. Perkins, *Surf. Sci.*, 2002, **497**, 155–165.

51 S. Y. Chin, C. T. Williams and M. D. Amiridis, *J. Phys. Chem. B*, 2006, **110**, 871–882.

52 L.-Y. Gan and Y.-J. Zhao, *J. Chem. Phys.*, 2010, **133**, 094703.

53 X. Wang, H. Shi, J. H. Kwak and J. Szanyi, *ACS Catal.*, 2015, **5**, 6337–6349.

54 K. Ito and H. J. Bernstein, *Can. J. Chem.*, 1956, **34**, 170–178.

55 L. Falbo, C. G. Visconti, L. Lietti and J. Szanyi, *Appl. Catal., B*, 2019, **256**, 117791.

56 A. de Klerk, *Chapter 4: Fischer Tropsch Synthesis in Fischer–Tropsch Refining*, 2011.

57 B. H. Davis, *Catal. Today*, 2009, **141**, 25–33.

58 B. T. Loveless, C. Buda, M. Neurock and E. Iglesia, *J. Am. Chem. Soc.*, 2013, **135**, 6107–6121.

59 S. Xu, S. Chansai, S. Xu, C. E. Stere, Y. Jiao, S. Yang, C. Hardacre and X. Fan, *ACS Catal.*, 2020, **10**, 12828–12840.

60 J. A. Onwudili and P. T. Williams, *Green Chem.*, 2010, **12**, 2214.